

# Design of Precision Positioner with Hall-effect Sensors and Multivariable Control Methodology

Ho Yu\* and Won-jong Kim

**Abstract:** This paper presents the design and multivariable feedback control of a compact precision positioner. The moving stage that has a total mass of 1.52 kg can generate all 6-axis motions with a single frame. Aerostatic bearings levitate the positioner and three 3-phase synchronous permanent-magnet planar motors (SPMPMs) generate electromagnetic forces over the concentrated-field permanent-magnet matrix. Three Hall-effect sensors measure the magnetic flux to calculate the planar position and three laser-distance sensors detect the vertical displacement. Real Time Application Interface (RTAI) with Comedi on a Linux personal computer is used for real-time control. Single-input single-output (SISO) digital lead-lag controllers for each axis are designed, and a multi-input multi-output (MIMO) model is developed for the positioner. Reduced-order linear-quadratic-Gaussian (LQG) controllers are applied in horizontal positioning. Several experimental results demonstrate the dynamic performance of the positioner.

**Keywords:** Hall-effect sensor, multivariable control, precision manufacturing, real-time digital control, reduced-order LQG, RTAI.

## 1. INTRODUCTION

In modern electronics, microchips are commonly used in computer boards, cellular phones, and many other devices. In the semiconductor manufacturing process, the computer chips require high-density storage capabilities to process a vast amount of information, and the chip manufacturing industry offered a 20-nm lithography technology in 2014 [1]. For photolithography-based processing, a wafer stepper is utilized as a crucial piece of equipment. Step-and-repeat motions are the basic movement in the wafer stepper [2].

The industry uses various types of positioners to meet the requirement of the positioning system. Positioning stages are classified by their motion range and accuracy such as being a long-range scanning positioner or a high-precision positioner. In planar motion control, crossed-axis or gantry positioners are common types. However, traditional positioners suffer from significant drawbacks including being unable to inherently generate rotational motions and the high manufacturing cost due to its mechanical bearing tolerance. Since they need an extra mechanical device for an additional axis control, the positioner structure becomes complicated and bulky.

A planar motor can be used for the wafer stepper stage. Generating multi-dimensional precision motion with a

large travel range is a significant advantage of the planar motor. The early planar motor proposed by Sawyer [3] is a variable-reluctance type and was commercialized by Northern Magnetics and Megamation [4]. It provides the position repeatability of the order of  $5\ \mu\text{m}$ . However, it requires a tight air gap of  $25\ \mu\text{m}$  and ultra-fine surface finish. Large cogging force, overheating, and excessive attraction force are the key drawbacks of the Sawyer motor.

Hinds and Nocito [5], and Pelta [6] advanced the Sawyer motor system. In their designs, the planar motor contains a set of permanent-magnet cubes as a stator, rather than the iron protrusions in the base plate of a Sawyer motor. The first permanent-magnet planar motor that employed orthogonally superimposed conventional one-dimensional magnet arrays was proposed by Asakawa [7]. Jansen, *et al.* designed a moving-magnet planar actuator, which had herringbone-pattern coils based on a Halbach magnet array [8]. Ueda and Ohsaki proposed a three-degree-of-freedom (3-DOF) planar actuator with a small mover capable of making large yaw and translational displacements [9]. Piezoelectric materials can also be used as an actuator in precision motion control. Young *et al.* developed a flexure-based  $xy$  stage for fast nanoscale positioning [10]. It generated a repeatable nanometer resolution with a high bandwidth with less wear, backlash, and friction. Low cost and low cross-coupling among axes are

Manuscript received December 25, 2014; revised April 8, 2015; accepted June 11, 2015. Recommended by Associate Editor Do Wan Kim under the direction of Editor Myotaeg Lim.

Ho Yu is with POSCO Technical Research Laboratories, Geodong-dong, Nam-gu, Pohang, Gyeongbuk 790-300, Korea (e-mail: jameskaten@gmail.com). Won-jong Kim is with the Department of Mechanical Engineering, Texas A&M University, College Station, TX 77843-3123, USA (e-mail: wjkim@tamu.edu).

\* Corresponding author.

the key advantages of the stage. However, it has a limited motion travel range.

In this paper, we propose a compact multi-dimensional positioner with the synchronous permanent-magnet planar motor (SPMPM), which is composed of 3 phase armatures. The three SPMPMs on the bottom of the positioner generate translational and vertical forces by automated current-phase control. There is a superimposed Halbach magnet-matrix as a stator on the base plate of the positioning stage. Since the positioner has a contactless frame levitated by aerostatic bearings, mechanical friction, coupling, and lubricant do not exist.

The rest of paper is organized as follows: The design of the precision positioner is introduced in Section 2. The Hall-effect sensors and the positioning methodologies are expressed in Section 3. A Linux-based real-time system with RTAI and Comedi is illustrated in Section 4. Dynamic modeling based on force allocations and multivariable dynamic controllers are developed in Section 5, and the conclusion is given in Section 6.

## 2. MECHANICAL DESIGN

The stage is composed of the moving part with armature coils, magnet blocks to generate sinusoidal magnetic field, levitation apparatus, and sensors in Fig. 1. Its overall dimension is  $170.18 \times 152.40 \times 53.34$  mm. A moving part, namely the platen, was manufactured with a single triangular frame. The absence of mechanical contact generates no backlash and dynamic coupling, so that a simple dynamic model is applied for the motion control. In order to reduce the mass, most parts including the main body, aerostatic bearing holders, and sensor mounts were manufactured with Delrin, which has the mass density of  $1.54 \text{ g/cm}^3$ . The overall mass of the platen is 1.52 kg without the power cables.

The main difference compared to the prior arts is applying Hall-effect sensors in precision control. Three Hall-effect sensors detect horizontal motions over the magnet blocks. Vertical displacements are detected by laser distance sensors (Nanogage 100). All six-axis motions are generated by the three 3-phase synchronous planar motor. Two windings at the bottom of the triangular frame in Fig. 2 generate the driving forces in  $y$ , and the one at the top generates the driving force in  $x$ . All three windings generate magnetic suspension forces at the same time. The planar motors provide not only levitation forces but also rotation motions of roll, pitch, and yaw. Table 1 presents the specifications of the planar motor.

The superimposition of two orthogonal Halbach magnet arrays in the base plate produces a concentrated-field magnet matrix [2] that is used as a stator. The magnetic field generated by this magnet matrix is measured by 2-axis Hall-effect sensors to determine the platen's unique position in the plane [11]. As the concentrated-field mag-

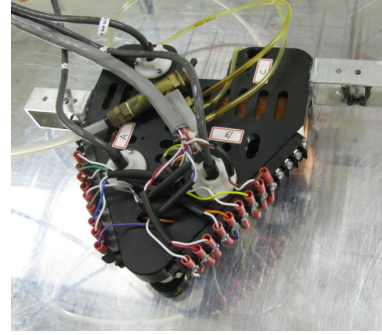


Fig. 1. Photograph of the platen.

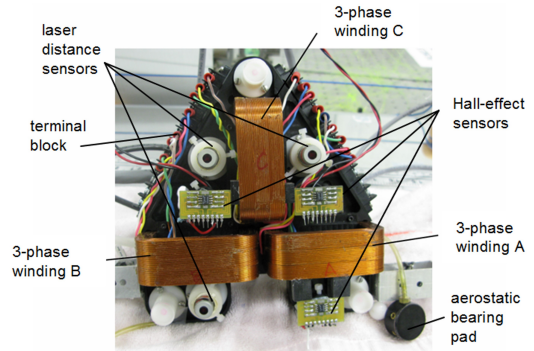


Fig. 2. The bottom face of the platen.

Table 1. Parameters of the planar motor armatures.

Specifications	Values
Number of phases	3
Pitch, $l$	$50.977 \text{ mm} = 2.007''$
Number of turns in the coil	305
Cross-sectional area of a winding	$8.6524 \times 10^5 \text{ m}^2$
Winding thickness, $\Gamma$	15
Phase inductance	15.264 mH
Phase resistance	$4.98 \Omega$
Nominal phase current	0.5674 A
Maximum phase current	1.26 A
Nominal phase voltage	2.837 V
Maximum phase voltage	6.525 V
Turn density, $\eta_0$	$3.5246 \times 10^6 \text{ turns/m}^2$
Nominal peak current density	$2 \times 10^6 \text{ A/m}^2$

net matrix follows the linear superposition of two orthogonal magnet arrays, the basic working principle of the Halbach magnet array is applicable to the two-dimensional magnet matrix. Higher power efficiency than that of conventional magnetization patterns can be achieved by using this magnet matrix in the stationary base plate.

One of the components in determining the maximum travel range of the positioner is the size of the magnet matrix. The magnet matrix consists of 6 pitches in the  $x$ - and

Table 2. Parameters of the magnet matrix.

Specifications	Values
Magnet array width, $w$	12.7 mm
Nominal motor air gap, $z_0$	2.3 mm
Magnet matrix size	$304.8 \times 304.8$ mm
Magnet thickness, $\Delta$	$l/4$
Equivalent magnet remanence	$\mu_0 M_o = 0.71$ T
Fundamental wave number	$\gamma_1 = 2\pi/l = 123.25$ m <sup>-1</sup>

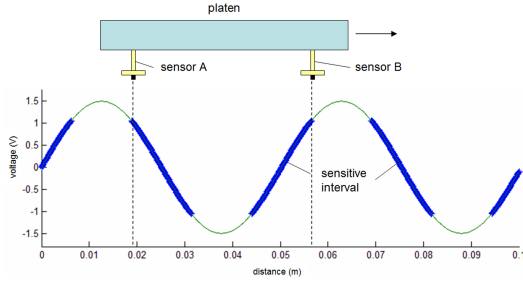


Fig. 3. Illustration of the sensor switching and collaboration principle: Sensor A enters and sensor B leaves the sensitive intervals.

$y$ -directions, respectively. By increasing the number of pitches in each direction, the travel range of the positioner can be easily extended. Table 2 summarizes the magnet-matrix parameters.

### 3. HALL-EFFECT SENSORS

In prevailing precision motion stages, laser interferometers are commonly used as position sensors due to their high resolution. However, the positioner in this paper employed the 2-axis Hall-effect sensors that provide unlimited travel range and large rotation angles [11]. Since a Hall-effect sensor has simple structure, it is not only cost-effective but also free from complicated sensor alignment.

#### 3.1. Hall-effect sensor and sensing methodology

Three 2-axis Hall-effect sensors (2D-VD-11SO, Sen-tron, AG) are used for lateral position measurement. Each Hall-effect sensor has two orthogonal sensing axes and measures the magnetic flux density in two independent perpendicular directions. The sensor has a magnetic sensitive volume of  $0.25 \times 0.25 \times 0.25$  mm and a sensitivity of 400 mV/T. The position of the platen cannot be detected by a single sensor, because a sinusoidal magnetic flux density in one pitch includes two identical points of magnitude. To acquire the unique position or decide the direction of the platen, two or more sensors that measure a sinusoidal magnetic flux density are required in one axis.

Fig. 3 illustrates how the Hall-effect sensors collaborate to measure single-axis motion. The sinusoidal magnetic

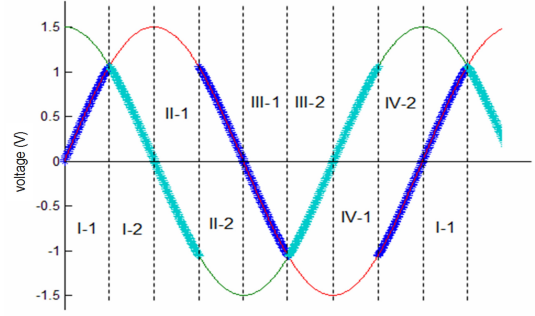


Fig. 4. Sensor position arrangement.

flux density is converted to the voltage signal. The Hall-effect sensors do not obtain data from the entire period in the sinusoidal wave. Each sensor detects the magnetic flux density in the sensitive intervals in Fig. 3, and more than one sensor in one axis motion calculate a positioner's location continuously. Sensor B steps out from the sensitive interval and Sensor A enters the sensitive interval simultaneously. This sensor switching takes place repeatedly when the platen moves over a pitch. One of the two sensors always covers the sensitive intervals presented by the thicker lines in Fig. 3. The sensitive interval denotes the section that has the large gradient of magnetic flux density with respect to the position. The sensitive intervals are required to be connected over a sinusoidal magnetic flux wave as in Fig. 4. Two sinusoidal voltage waves from two adjacent Hall-effect sensors has  $90^\circ$  phase difference, and each sensitive interval in two waves allows the platen to move continuously. Phase differences between two sensors are caused by a sensor position gap of

$$(0.25 + 0.5n) \times \text{pitch}, \quad n = 1, 2, 3, \dots \quad (1)$$

Sensor switching is also required at every quarter pitch. Each Hall-effect sensor that has dual channels measures two orthogonal directions, and three Hall-effect sensors produce a total of six voltage readings. Four voltage readings,  $V_{ax}$  and  $V_{bx}$  in  $x$ ,  $V_{ay}$  and  $V_{cy}$  in  $y$  are used to determine the unique position in translation motions. Rough voltage data readings directly from the Hall-effect sensor are required to be normalized in every pitch. Accurate position measurement depends on the calibration of normalization.

$$a_x = \sin(\omega_{ax} V_{ax} + V_{axoffset}) \quad (2)$$

$$b_x = \sin(\omega_{bx} V_{bx} + V_{bxoffset}) \quad (3)$$

The values of  $a_x$  and  $b_x$  are the sine values from the normalized data in  $x$ . The calibration constants in  $x$  are  $w_{ax}$  and  $w_{bx}$ , and  $V_{axoffset}$  and  $V_{bxoffset}$  are the offset values for each sensor. Voltage equations in  $y$  has the same format with those in the  $x$ -direction.

$$\Delta x_d = \alpha \Delta x_a + \beta \Delta x_b, \quad (4)$$

$$\Delta y_d = \alpha \Delta y_a + \beta \Delta y_c, \quad (5)$$

where  $\Delta x_a$  and  $\Delta x_b$  are the time derivative terms of  $a_x$  and  $b_x$ . There are 8 sections in one cycle in Fig. 4. Each section uses different combinations of the Hall-effect sensors in order to obtain data only from the sensitive intervals. The scaling factor,  $\alpha$  and  $\beta$  are then used.

### 3.2. Filtering

The noise must be filtered out from the position data obtained from the Hall-effect sensors. Hence, a recursive Kalman filter was introduced. The Kalman filter can not only filter out the Hall-effect sensor noise but also estimate the velocity states in  $x, y$ , and  $\phi$ . The state vector is

$$\bar{k} = \begin{bmatrix} x & y & \phi \end{bmatrix}^T. \quad (6)$$

The filter dynamic model in the continuous time is presented as follows:

$$\begin{bmatrix} \dot{\bar{k}}(t) \\ \ddot{\bar{k}}(t) \\ \ddot{\bar{k}}(t) \end{bmatrix} = \begin{bmatrix} 0 & I_{3 \times 3} & 0 \\ 0 & 0 & I_{3 \times 3} \\ 0 & 0 & 0 \end{bmatrix} \begin{bmatrix} \bar{k}(t) \\ \dot{\bar{k}}(t) \\ \ddot{\bar{k}}(t) \end{bmatrix} + \begin{bmatrix} 0 \\ 0 \\ I_{3 \times 3} \end{bmatrix} \bar{w}(t), \quad (7)$$

$$\tilde{y}(t) = \begin{bmatrix} I_{3 \times 3} & 0 & 0 \end{bmatrix} \begin{bmatrix} \bar{k}(t) \\ \dot{\bar{k}}(t) \\ \ddot{\bar{k}}(t) \end{bmatrix} + \bar{\theta}(t), \quad (8)$$

where values of  $\bar{w}$  and  $\bar{\theta}$  are the process noise and the measurement input noise from the Hall-effect sensors, which are assumed as zero-mean Gaussian.

$$\bar{\theta}(t) \sim N(0, R_k), \quad (9)$$

where the noise covariance coming from the Hall-effect sensors was measured by experiments on the order of  $5 \times 10^{-5}$  m. The discrete-time dynamic model is

$$\bar{x}_n = \begin{bmatrix} \bar{k} & \dot{\bar{k}} & \ddot{\bar{k}} \end{bmatrix}^T, \quad (10)$$

$$\bar{x}_{n+1} = \begin{bmatrix} I_{3 \times 3} & (\Delta t)I_{3 \times 3} & \frac{1}{2}(\Delta t)^2 I_{3 \times 3} \\ 0 & I_{3 \times 3} & (\Delta t)I_{3 \times 3} \\ 0 & 0 & I_{3 \times 3} \end{bmatrix} \bar{x}_n + \begin{bmatrix} \frac{1}{6}(\Delta t)^3 I_{3 \times 3} \\ \frac{1}{2}(\Delta t)^2 I_{3 \times 3} \\ (\Delta t)I_{3 \times 3} \end{bmatrix} \bar{w}_n = A\bar{x}_n + \Gamma\bar{w}_n, \quad (11)$$

$$\tilde{y}_n = \begin{bmatrix} I_{3 \times 3} & 0 & 0 \end{bmatrix} \bar{x}_n + \bar{\theta}_n = C\bar{x}_n + \bar{\theta}_n, \quad (12)$$

where  $\Delta t$  is the integration interval in real-time control. The error covariance matrix  $Q$  from the process noise  $\bar{w}$ , which is the positive constant matrix, is presented as

$$Q = \begin{bmatrix} q_x & 0 & 0 \\ 0 & q_y & 0 \\ 0 & 0 & q_\phi \end{bmatrix} = \begin{bmatrix} 100 & 0 & 0 \\ 0 & 100 & 0 \\ 0 & 0 & 10^5 \end{bmatrix}. \quad (13)$$

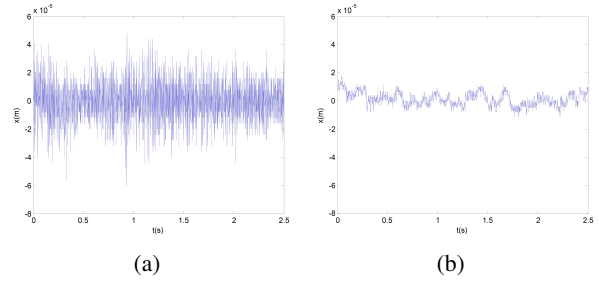


Fig. 5. Zero position outputs in  $x$ : (a) Hall-effect sensor data and (b) after filtering.

The bandwidth of the Kalman filter was set at 50 Hz in  $x$  and  $y$ , and at 100 Hz in the rotation around  $z$ .

$P$  is the covariance matrix of the optimal estimation error. The initial value of  $p_0 = 1 \times 10^8$  m<sup>2</sup> was determined by experiments to obtain good convergence.

$$P_{n+1} = AP_nA^T + \Gamma Q \Gamma^T \quad (14)$$

$$P_0 = p_0 I_{9 \times 9} \quad (15)$$

Then gain matrix is expressed as

$$K_n = P_n C^T (C P_n C^T + R)^{-1}. \quad (16)$$

Figs. 5 (a) and (b) illustrate the outputs from the Hall-effect sensors with the zero position in  $x$  and after the Kalman filtering, respectively. The noise levels of Figs. 5(a) and (b) are around  $\pm 4 \times 10^{-5}$  m and  $\pm 1 \times 10^{-5}$ , where the noise magnitude has been reduced by 75%.

## 4. CONTROL SOFTWARE

### 4.1. RTAI and Comedi

Linux Ubuntu, which supports real-time user interface as an open-source, was used as an OS to perform real-time tasks for the precision positioner. Ubuntu not only has well developed tools and graphic interface but also supports various hardware application. Real-Time Application Interface (RTAI) is a kernel-modified package of Linux. It supports time critical components needed for real-time control and is suitable for the hard real-time system that needs to be preemptive and deterministic. Comedi stands for Control and Measurement Device Interface. Comedi is used to achieve the input and output (I/O) interface with the hardware components such as the positioners, amplifiers, and the data acquisition boards. A standard Linux kernel and RTAI can be used with Comedi. It can be used to develop tools, libraries, and drivers for the data acquisition boards. There are two Comedi packages: Comedi and Comedilib. Comedi implements the kernel space functionality, and Comedilib is applied for the user space access for using the device functions.

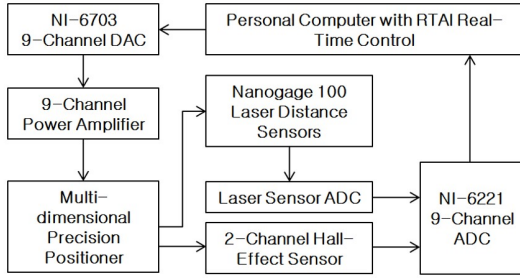


Fig. 6. Diagram of the control structure.

#### 4.2. Control structure

Fig. 6 shows a schematic diagram of the control structure of the positioning system. This diagram generally illustrates the process of the control and sensor signals. The real-time control system running on the PC acquires analog data from sensors such as laser distance sensors and 2-axis Hall-effect sensors through the analog-to-digital converter (ADC) board (NI-6221). The control algorithm in conjunction with RTAI and Comedi functions processes all the position measurement data and computes the control outputs to operate the compact 6-DOF positioner in real time. The user interface to control the position and velocity of the platen was developed in the C language. The position command data computed from the PC flow to the digital-to-analog converters (DACs) on NI-6703, which supports sixteen 16-bit analog output voltage channels with  $\pm 10$  V and 8 digital I/O lines. Nine independent control output signals from the DACs go into the power amplifiers. The power amplifiers supply commanded phase currents to each planar motor winding. As a result, actuation forces to control the movement of the platen are generated by the three planar motors.

### 5. MODELING AND CONTROLLER DESIGN

#### 5.1. Linearized force equation

The SPMPMs are the Lorents-force-type actuator. The Lorentz force law,  $\vec{F} = \vec{J} \times \vec{B}$  was employed to derive the driving force and the suspension force using the Maxwell stress tensor methodology. Each planar motor with three phases can generate the horizontal magnetic force and the vertical magnetic force by a DQ decomposition method.

The decoupled forces in both the driving and suspension directions are derived by the electromagnetic analysis as follows [2, 12]:

$$\begin{bmatrix} f_y \\ f_z \end{bmatrix} = \frac{1}{2} \mu_0 M_0 \eta_0 N_m G e^{-\gamma_{z_0}} \times \begin{bmatrix} \cos \gamma_{1y} & \sin \gamma_{1y} \\ -\sin \gamma_{1y} & \cos \gamma_{1y} \end{bmatrix} \begin{bmatrix} \frac{2}{3} & -\frac{1}{3} & -\frac{1}{3} \\ 0 & \frac{1}{\sqrt{3}} & -\frac{1}{\sqrt{3}} \end{bmatrix} \begin{bmatrix} i_A \\ i_B \\ i_C \end{bmatrix}, \quad (17)$$

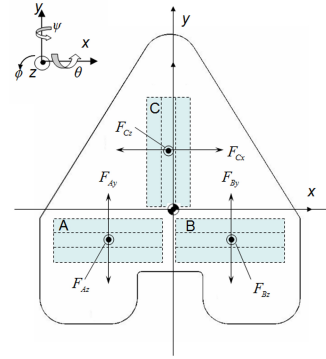


Fig. 7. Individual force components generated by motor A, B, and C.

Table 3. 6-DOF motion generation.

	Motor A	Motor B	Motor C
$x$	$-F_{Ay}$	$F_{By}$	$F_{Cx}$
$y$	$F_{Ay}$	$F_{By}$	0
$z$	$F_{Az}$	$F_{Bz}$	$F_{Cz}$
$\phi$	$-F_{Ay}$	$F_{By}$	0
$\theta$	$-F_{Az}$	$-F_{Bz}$	$F_{Cz}$
$\psi$	$F_{Az}$	$-F_{Bz}$	0

where the variables of the electromagnetic design are introduced in Tables 1 and 2.

The total horizontal force and the vertical force are represented as  $[f_y \ f_z]^T$  with respect to the motor phase currents  $[i_A \ i_B \ i_C]^T$ . Phase differences among windings in the planar motor are  $\pi/3$ . The motor geometric constant  $G$  is  $1.072 \times 10^{-5} \text{ m}^3$ . Motor C has a similar magnetic force equation in  $[f_y \ f_z]^T$  with the symmetry of the concentrated-field magnet matrix.

The decoupled force equations are applied to each planar motor in Fig. 7. To generate all six independent motions, the system requires at least six individual actuators. All three planar motors together can generate any directional motions by interactions among planar motors explained in Table 3.

#### 5.2. Controllers

The positioner is regarded as a pure mass system without friction between the mover and the ground. The equations of motion based on Newton's second law in the horizontal modes are as follows:

$$M \frac{d^2 x}{dt^2} = f_x, \quad M \frac{d^2 y}{dt^2} = f_y, \quad I_{zz} \frac{d^2 \phi}{dt^2} = M_{oz}. \quad (18)$$

The dynamic models for vertical modes are as follows:

$$M \frac{d^2 z}{dt^2} = f_z - K_z z, \quad (19)$$

$$I_{xx} \frac{d^2 \theta}{dt^2} = M_{ox} - K_\theta \theta, \quad I_{yy} \frac{d^2 \psi}{dt^2} = M_{oy} - K_\psi \psi, \quad (20)$$

where  $M$  is the total mass of 1.52 kg and the magnetic modal forces are represented by  $f$ . The principal moments of inertia  $I_{xx}$ ,  $I_{yy}$ , and  $I_{zz}$  are 0.0037, 0.0019, and 0.0022 kg·m<sup>2</sup>, respectively. The effective spring constant of the motor is  $K_z = 620$  N/m, which is determined by experiments based on Hooke's law.  $K_\theta$  and  $K_\psi$  are the effective torsional spring constants, which are 65 and 87 N·m/rad by experiments.

Second-order digital controllers were designed with the dynamic models in all axes as (21)–(22). The sampling frequency of 1 kHz was determined by the experiments with respect to the hardware setup.

$$G_{x,y}(s) = 1.5 \times 10^4 \left( \frac{1 + 0.11s}{1 + 0.00088s} \right) \left( \frac{1 + 0.1s}{s} \right) \quad (21)$$

$$G_\phi(s) = 35 \left( \frac{1 + 0.12s}{1 + 0.00088s} \right) \left( \frac{1 + 0.1s}{s} \right). \quad (22)$$

The crossover frequencies in the horizontal mode are 25.27 and 22.4 Hz with the phase margins of 73.1° and 66.3°, respectively. Similarly, the vertical-mode controllers were designed as follows.

$$G_z(s) = 323252 \left( \frac{s + 102.91}{s + 776.828} \right) \left( \frac{s + 10}{s} \right), \quad (23)$$

$$G_\theta(s) = 900 \left( \frac{s + 80.0413}{s + 604.199} \right) \left( \frac{s + 10}{s} \right), \quad (24)$$

$$G_\psi(s) = 1100 \left( \frac{s + 80.0413}{s + 604.199} \right) \left( \frac{s + 10}{s} \right). \quad (25)$$

Pure integrators located at  $s = 0$  eliminate the steady-state error coming from aerostatic bearings and umbilical cables.

Closed-loop step responses of 20- $\mu$ m in  $x$ , 100- $\mu$ m in  $y$ , and 0.01° in  $\theta$  are shown in Fig. 8. Step responses in the experimental results demonstrate that the rise time is less than 25 ms, the maximum overshoot is around 20%, and the settling time is less than 220 ms without steady-state errors in  $x$  and  $y$ . The position noise is 6  $\mu$ m rms in  $x$  and  $y$ , which is mainly caused from the Hall-effect sensors.

Planar motions in a long range are commonly used in precision-positioning applications, such as microlithography and scanning microscopy. The maximum travel ranges of this positioner are 220 mm in  $x$  and 200 mm in  $y$ . They are only limited by the number of pitches in the magnet matrix. The platen's geometric asymmetry accounts for the difference in the maximum travel ranges in  $x$  and  $y$ . A large circular motion of 200-mm diameter in Fig. 9 was achieved experimentally. The angular velocity was 0.2094 rad/s in this circular motion.

### 5.3. Multivariable controllers

This section discusses multivariable control for the positioner. The LQG controller methodology is used for the

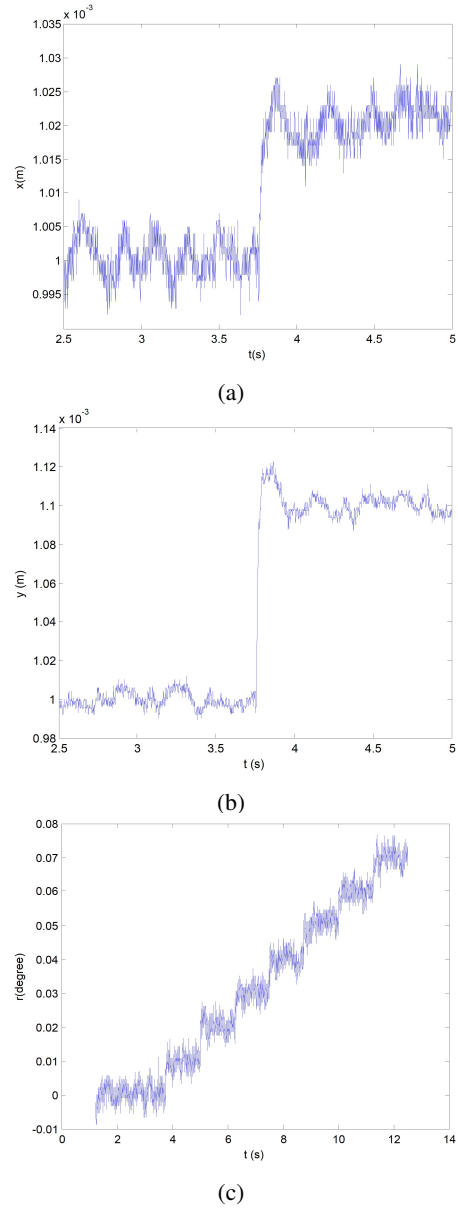


Fig. 8. (a) 20- $\mu$ m step response in  $x$ , (b) 100- $\mu$ m step response in  $y$ , and (c) 0.01° step response in  $\phi$ .

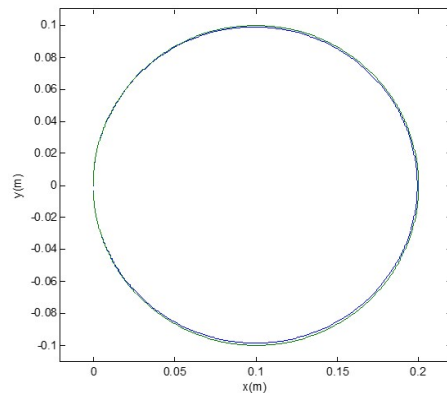


Fig. 9. 200-mm diameter circular motion.

lateral motion control. The state-space model of the positioner was derived in (26)-(27).

$$\begin{bmatrix} \dot{x} \\ \dot{y} \\ \dot{\phi} \\ \dot{d} \\ \dot{f} \\ \dot{v} \end{bmatrix} = \begin{bmatrix} 0 & 0 & 0 & 1 & 0 & 0 \\ 0 & 0 & 0 & 0 & 1 & 0 \\ 0 & 0 & 0 & 0 & 0 & 1 \\ 0 & 0 & 0 & 0 & 0 & 0 \\ 0 & 0 & 0 & 0 & 0 & 0 \\ 0 & 0 & 0 & 0 & 0 & 0 \end{bmatrix} \begin{bmatrix} x \\ y \\ \phi \\ d \\ f \\ v \end{bmatrix} + \begin{bmatrix} 0 & 0 & 0 \\ 0 & 0 & 0 \\ 0 & 0 & 0 \\ 0 & 0 & 13.2547 \\ 13.2547 & 13.2547 & 0 \\ -117.15 & 117.15 & 0 \end{bmatrix} \begin{bmatrix} i_{AQ} \\ i_{BQ} \\ i_{CQ} \end{bmatrix}, \quad (26)$$

$$Y_1 = \begin{bmatrix} 1 & 0 & 0 & 0 & 0 & 0 \\ 0 & 1 & 0 & 0 & 0 & 0 \\ 0 & 0 & 1 & 0 & 0 & 0 \end{bmatrix} \begin{bmatrix} x \\ y \\ \phi \\ d \\ f \\ v \end{bmatrix}. \quad (27)$$

The vector  $[x \ y \ \phi]^T$  presents the displacements of horizontal motions and the vector  $[d \ f \ v]^T$  indicates the velocities of  $[x \ y \ \phi]^T$ . Since Hall-effect sensors provide solely displacement values, an observer to estimate the velocity states is required in the system in order to achieve full state feedback. In the plant dynamics, if  $(A, B)$  is controllable and  $(A, C)$  is observable, an observer/state-feedback controller can be designed. The observer takes the original plant's input and output. An estimate of the plant's state vector is produced by the observer. The observer has identical structure with the plant with additional input  $y - \hat{y}$ .

$$\dot{\hat{x}} = A\hat{x} + Bu + L(y - \hat{y}) \quad (28)$$

$$\hat{y} = C\hat{x} + Du \quad (29)$$

The observer gain matrix  $L$  can be computed because  $(A, C)$  is observable. The closed-loop dynamics is represented with the state feedback of  $u = -K\hat{x}$

$$\begin{bmatrix} \dot{x} \\ \dot{\hat{x}} \end{bmatrix} = \begin{bmatrix} A & -BK \\ LC & A - BK - LC \end{bmatrix} \begin{bmatrix} x \\ \hat{x} \end{bmatrix}. \quad (30)$$

Since the original plant and the controller do not include the integrators, steady-state errors in the closed-loop position control may exist. To reduce the steady-state errors, three pure integrators are employed in the original system as follows:

$$\begin{bmatrix} \dot{x} \\ \dot{y} \\ \dot{\phi} \\ \dot{z}_1 \\ \dot{z}_2 \\ \dot{z}_3 \\ \dot{d} \\ \dot{f} \\ \dot{v} \end{bmatrix} = \begin{bmatrix} 0 & 0 & 0 & 0 & 0 & 0 & 1 & 0 & 0 \\ 0 & 0 & 0 & 0 & 0 & 0 & 0 & 1 & 0 \\ 0 & 0 & 0 & 0 & 0 & 0 & 0 & 0 & 1 \\ 1 & 0 & 0 & 0 & 0 & 0 & 0 & 0 & 0 \\ 0 & 1 & 0 & 0 & 0 & 0 & 0 & 0 & 0 \\ 0 & 0 & 1 & 0 & 0 & 0 & 0 & 0 & 0 \\ 0 & 0 & 0 & 0 & 0 & 0 & 0 & 0 & 0 \\ 0 & 0 & 0 & 0 & 0 & 0 & 0 & 0 & 0 \\ 0 & 0 & 0 & 0 & 0 & 0 & 0 & 0 & 0 \end{bmatrix} \begin{bmatrix} x \\ y \\ \phi \\ z_1 \\ z_2 \\ z_3 \\ d \\ f \\ v \end{bmatrix} + \begin{bmatrix} 0 & 0 & 0 \\ 0 & 0 & 0 \\ 0 & 0 & 0 \\ 0 & 0 & 13.2547 \\ 13.2547 & 13.2547 & 0 \\ -117.15 & 117.15 & 0 \end{bmatrix} \begin{bmatrix} i_{AQ} \\ i_{BQ} \\ i_{CQ} \end{bmatrix}, \quad (31)$$

$$+ \begin{bmatrix} 0 & 0 & 0 \\ 0 & 0 & 0 \\ 0 & 0 & 0 \\ 0 & 0 & 0 \\ 0 & 0 & 0 \\ 0 & 0 & 0 \\ 0 & 0 & 13.2547 \\ 13.2547 & 13.2547 & 0 \\ -117.15 & 117.15 & 0 \end{bmatrix} \begin{bmatrix} i_{AQ} \\ i_{BQ} \\ i_{CQ} \end{bmatrix}, \quad (31)$$

$$Y_1 = \begin{bmatrix} 1 & 0 & 0 & 0 & 0 & 0 & 0 & 0 & 0 \\ 0 & 1 & 0 & 0 & 0 & 0 & 0 & 0 & 0 \\ 0 & 0 & 1 & 0 & 0 & 0 & 0 & 0 & 0 \end{bmatrix} \begin{bmatrix} x \\ y \\ \phi \\ z_1 \\ z_2 \\ z_3 \\ d \\ f \\ v \end{bmatrix}. \quad (32)$$

The full-order state controller is inefficient and requires more computations. Thus, a reduced-order LQG controller is developed [12]. The full states are divided by two subsystems, which are the terms of known state  $x_1$  and the terms of unknown state  $x_2$ . By estimating only unknown states, the controller structure will be simpler. The unknown state vector  $x_2$  includes the velocity states ( $d$ ,  $f$ , and  $v$ ). The system is discretized at the sampling frequency of 800 Hz. The closed-loop dynamics of the reduced-order LQG controller is derived with the state-feedback control law  $u = -k_1x_1 - k_2\hat{x}_2$ .

$$\begin{bmatrix} \dot{x}_1 \\ \dot{x}_2 \\ \dot{x}_3 \end{bmatrix} = \begin{bmatrix} A_{11} - B_1k_1 - B_1k_2L \\ A_{21} - B_2k_1 - B_2k_2L \\ (A_{22} - LA_{12})L + A_{21} - LA_{11} - (B_2 - LB_1)(k_1 + k_2L) \\ A_{12} & -B_1k_2 \\ A_{22} & -B_2k_2 \\ 0 & A_{22} - LA_{12} - B_2k_2 + LB_1k_2 \end{bmatrix} \begin{bmatrix} x_1 \\ x_2 \\ x_3 \end{bmatrix}, \quad (33)$$

$$Y = [I \ 0 \ 0] \begin{bmatrix} x_1 \\ x_2 \\ x_3 \end{bmatrix}, \quad (34)$$

where  $x_3 = \hat{x}_2 - Lx_1$ , and  $\hat{x}_2$  denotes the estimates of the unknown states  $x_2$ . The estimator gain matrix is represented as  $L$ . The LQ gain matrix of  $K = [k_1 \ k_2]$  is also divided for the known state  $k_1$  and the estimated state  $k_2$ . Then, the new state matrix  $A$  can be derived as

$$\begin{bmatrix} A_{11} - B_1k_1 & A_{12} - B_1k_2 & -B_1k_2 \\ A_{21} - B_2k_1 & A_{22} - B_2k_2 & -B_2k_2 \\ 0 & 0 & A_{22} - LA_{12} \end{bmatrix} = \begin{bmatrix} A - BK & -Bk_2 \\ 0 & A_{22} - LA_{12} \end{bmatrix}. \quad (35)$$

The multivariable system using the model based control (MBC) can basically guarantee the stability of the system and design a proper loop shape when  $(A, B)$  is controllable

and  $(A, C)$  is observable. In addition, it partially guarantees the system dynamics performances, stability, and robustness.

The LQG methodology is the combination of optimal state estimation from the Kalman filter and optimal state feedback from the LQR methodology for a deterministic plant [13]. The measurement noise and the disturbance need to be stochastic with known statistical properties. The plant model has a structure as follows:

$$\dot{x}(t) = Ax(t) + Bu(t) + L\bar{w}(t), \tag{36}$$

$$y(t) = Cx(t) + \bar{\theta}(t), \tag{37}$$

where  $\bar{w}(t)$  and  $\bar{\theta}(t)$  are process and measurement input noises considered as stationary zero-mean Gaussian noises. The properties of expectation and covariance are

$$E\{\bar{w}(t)\} = 0, \text{Cov}\{\bar{w}(t), \bar{w}(t-\tau)\} = \Psi\delta(t-\tau), \Psi = \Psi^T > 0, \tag{38}$$

$$E\{\bar{\theta}(t)\} = 0, \text{Cov}\{\bar{\theta}(t), \bar{\theta}(t-\tau)\} = \Theta\delta(t-\tau), \Theta = \Theta^T > 0. \tag{39}$$

The Kalman filter can be designed when  $(A, L)$  is controllable and  $(A, C)$  is observable, and the Kalman filter dynamics is shown as

$$\dot{\hat{x}} = (A - HC)\hat{x} + Bu + Hy, \tag{40}$$

$$0 = A\Sigma + \Sigma A^T - \Sigma C^T \Theta^{-1} C \Sigma + L\Psi L^T, H = \Sigma C^T \Theta^{-1}, \tag{41}$$

$$H = \begin{bmatrix} 1600 & 0.0006 & 0.0006 & 1 & 0 & 0 \\ 0.0006 & 1600 & 0.0006 & 0 & 1 & 0 \\ 0.0006 & 0.0006 & 1600 & 0 & 0 & 1 \end{bmatrix}, \tag{42}$$

where  $H$  is the Kalman-filter gain matrix obtained with Matlab, and the stability of the Kalman filter depends on the eigenvalues of matrix  $A - HC$  in (40).  $\Sigma = \Sigma^T > 0$  satisfies a filter algebraic Ricatti equation (FARE) in (41) with a unique positive-semidefinite solution. An optimal control law  $u = -K\hat{x}(t)$  is considered to minimize the cost function  $J$ .

$$J = E \left\{ \lim_{T \rightarrow \infty} \frac{1}{T} \int_0^T [x^T Q x + u^T R u] dt \right\} \tag{43}$$

The gain matrix  $K$  is determined by the control algebraic Ricatti equation (CARE).  $P$  is the unique positive-semidefinite solution of the CARE in (45).

$$K = R^{-1} B^T P \tag{44}$$

$$A^T P + PA - PBR^{-1} B^T P + Q = 0, P = P^T > 0 \tag{45}$$

The noise in channels and the output noise are assumed as

$$L = \text{diag}([1 \ 1]), \Theta = 5 \times 10^{-5} \text{diag}([1 \ 1]). \tag{46}$$

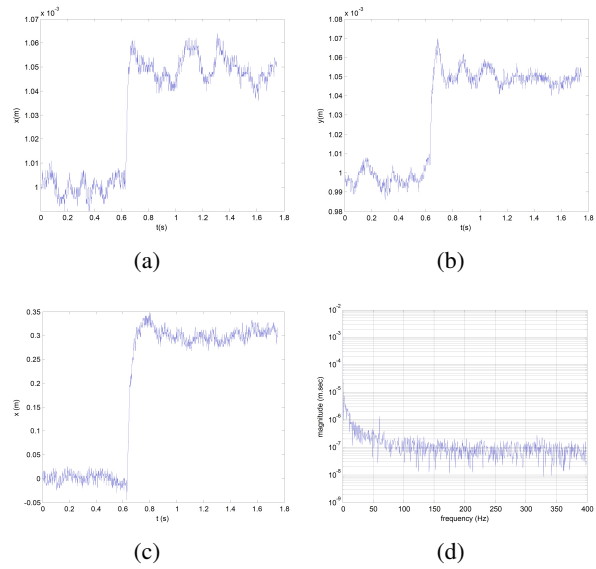


Fig. 10. 50- $\mu\text{m}$  step responses by LQG controller (a) in  $x$  and (b) in  $y$ . (c) 0.3 $^\circ$  step response in rotation around  $z$  and (d) FFT of (a).

The  $Q$  and  $R$  can be designed by the LQR state feedback method, because the  $(A, B)$  is stabilizable.

$$Q = \text{diag}([1e3 \ 1e4 \ 1e3 \ 1e9 \ 1e8 \ 1e8 \ 1e2 \ 1e2 \ 1e2]) \tag{47}$$

$$R = \text{diag}([1 \ 1 \ 1]) \tag{48}$$

The integrator-state weights have much higher values to remove the steady-state errors. The optimal gain matrix  $K$  can be calculated by the LQR methodology using the Matlab command “lqrd.”

$$K = \begin{bmatrix} 0 & 507.24 & -472.64 & 0 & 19975 \\ 0 & 507.24 & 472.64 & 0 & 19975 \\ 1757.55 & 0 & 0 & 84872 & 0 \\ -41394 & 0 & 64304 & -26962 & \\ 41394 & 0 & 64304 & 26962 & \\ 0 & 181556 & 0 & 0 & 0 \end{bmatrix} \tag{49}$$

Fig. 10 presents the step responses of the horizontal mode with the LQG compensator. Step responses of 50  $\mu\text{m}$  in both  $x$  and  $y$  are shown in Figs. 10(a) and (b), respectively. Fig. 10(c) presents the 0.3 $^\circ$  step response in rotation around  $z$ . A fast Fourier transform (FFT) of the step responses in  $x$  is presented in Fig. 10(d) and exhibits no dominant noise frequency component in the system. Step responses with the LQG controller have a position noise of 10  $\mu\text{m}$  rms. The position noise is mainly caused by the Hall-effect sensors. Besides it might be generated by the umbilical cables, three aerostatic bearings that blow air, the modeling error from dynamic analysis, and the inaccurate digital compensators.

## 6. CONCLUSION

In this paper, we presented the design and control of a compact precise multi-dimensional positioner. A 1.52 kg single moving stage based on SPMPMs and a concentrated-field magnet matrix generates multi-axis precision motions. Three 2-axis Hall-effect sensors measure the magnetic flux to calculate the unique position of the platen in horizontal directions. Unrestricted translations based on the size of the magnet array are one of the key advantages of employing the Hall-effect sensors. Small-size sensors make the positioner compact and light so that it can generate faster and cleaner dynamics.

The positioner was controlled by a Linux-based real-time system with RTAI and Comedi. Digital lead-lag compensators were designed for each axis, and a multivariable feedback controller based on the LQG methodology in the horizontal modes was applied on this system. Since the Hall-effect sensors only provide the position displacement data without velocity states, a recursive Kalman filter was used to estimate the remaining states. It also achieved better position estimation from the sensor signals including noise and disturbance. A reduced-order LQG methodology was used for a simple structure and fast computation. With several experiments, this compact multi-dimensional positioner demonstrated its suitability for potential applications in the precision-positioning industry.

## REFERENCES

- [1] Samsung Industry's first 20nm-class DDR3 DRAM—EETimes," [http://www.eetimes.com/author.asp?-doc\\_id=1321629](http://www.eetimes.com/author.asp?-doc_id=1321629)
- [2] H. Yu and W.-J. Kim, "A compact Hall-effect-sensing 6-DOF precision positioner," *IEEE/ASME Transactions on Mechatronics*, vol. 15, no. 6, pp. 982-985, December 2010. [click]
- [3] B. A. Sawyer, "Magnetic Positioning Device," U.S. Patent 3 376 578, April 2, 1968. [click]
- [4] Megamation, [http://www.megamation.com/hm\\_frame.htm](http://www.megamation.com/hm_frame.htm), 2001.
- [5] W. E. Hinds and B. Nocito, "The Sawyer linear motor," *Proc. of The Second Symposium on Incremental Motion Control Systems and Devices*, pp. W-1–W-10, 1973.
- [6] E. R. Pelta, "Two axis sawyer motor for motion systems," *IEEE Control System Magazine*, vol. 7, no. 5, pp. 20-24, October 1987. [click]
- [7] T. Asakawa, "Two dimensional precise positioning devices for use in a semiconductor apparatus," U.S. Patent 4 535 278, August 1985.
- [8] J. W. Jansen, C. M. M. van Lierop, A. Lomonova, and A. J. A. Vandenput, "Magnetically levitated planar actuator with moving magnet," *IEEE Trans. on Industry Applications*, vol. 44, no. 4, pp. 1108-1115, July/August 2008. [click]
- [9] Y. Ueda and H. Ohaski, "A planar actuator with a small mover traveling over large yaw and translational displacements," *IEEE Trans. on Magnetics*, vol. 44, no. 5, pp. 609-616, May 2008. [click]
- [10] Y. K. Young, S. S. Aphale, and S. O. R. Moheimani, "Design, identification, and control of a flexure-based xy stage for fast nanoscale positioning," *IEEE Trans. on Nanotechnol.*, vol. 8, no. 1, pp. 46-53, January 2009.
- [11] Y. Kawato and W.-J. Kim, "Multi-degree-of-freedom precision position sensing and motion control using two-axis Hall-effect sensors," *Journal of Dynamic Systems, Measurement and Control*, vol. 128, issue 4, pp. 980-988, December 2006. [click]
- [12] T. Hu and W.-J. Kim, "Modeling and multivariable control of a novel multi-dimensional levitated stage with high precision," *International Journal of Control, Automation, and Systems*, vol. 4, no. 1, pp. 1-9, February 2006.
- [13] L. Dai, "Filtering and LQG problems for discrete-time stochastic singular system," *IEEE Transactions on Automatic Control*, vol. 34, no. 10, pp. 1105-1108, October 1989. [click]



**Ho Yu** received the B.S. degree in mechanical engineering from Hanyang University, Seoul, Korea, in 2003 and the M.S. and Ph.D degrees in mechanical engineering from Texas A&M University, College Station, in 2005 and 2009, respectively. He is currently a research engineer in POSCO Robot Research Project Department. His research interests include precision position control and force control in robotics.



**Won-jong Kim** received the B.S. (*summa cum laude*) and M.S. degrees in control and instrumentation engineering from Seoul National University, Seoul, Korea, in 1989 and 1991, respectively, and the Ph.D. degree in electrical engineering and computer science from the Massachusetts Institute of Technology (MIT), Cambridge, in 1997. Since 2000, he has been with the Department of Mechanical Engineering, Texas A&M University (TAMU), College Station, where currently he is Associate Professor and was the inaugural Holder of the Gulf Oil/Thomas A. Dietz Career Development Professorship II in 2007–2010. His current research interests include the analysis, design, and real-time control of mechatronic systems, networked control systems, and nanoscale engineering and technology. He is the holder of three U.S. patents on precision positioning systems. He is Fellow of ASME, Senior Member of IEEE, and Member of Pi Tau Sigma. Prof. Kim is Associate Editor of *International Journal of Control, Automation, and Systems*, and *Asian Journal of Control*, and was Associate Editor of *ASME Journal of Dynamic Systems, Measurement and Control* and Technical Editor of *IEEE/ASME Transactions on Mechatronics*.